Resolution Enhancement by Subpixel Sampling and Computational Reconstruction

JONATHAN BREWER[1], MILAD ALMASIAN[1], ALIREZA SABERIGARAKANI[1], XINYUAN ZHANG[1], FENGHUA SHI[1], YICHEN DING[1, 2, 3,*]

[1]Department of Bioengineering, The University of Texas at Dallas, Richardson, TX 75080, USA
[2]Center for Imaging and Surgical Innovation, The University of Texas at Dallas, Richardson, TX 75080, USA
[3]Hamon Center for Regenerative Science and Medicine, UT Southwestern Medical Center, Dallas, TX 75390, USA
[*]yichen.ding@utdallas.edu

Receipt of publication:

Image resolution and field-of-view in far-field optical microscopy are often inversely proportional to one another due to digital sampling limitations imposed by the magnification of the system and the pixel size of the sensor. We present a method including a spatial shifting mechanism and a reconstruction algorithm that bypasses this tradeoff by shifting the sample to be imaged by subpixel increments, before registering the images via phase correlation and combining the resulting registered images using the shift-and-add approach. Importantly, this method requires no specific optical components that are uncommon to commercially available or custom-built microscope systems. The findings of the presented study demonstrate an improvement to spatial resolution of ~42% while maintaining the system's field-of-view (FOV), leading to a more than 2-fold improvement to the system's space-bandwidth product.

In traditional far-field optical microscopy, the space-bandwidth product (SBP) is often used as a qualitative ratio to determine the information-carrying capacity of an image, often defined as $FOV/Resolution^2$ [1]. However, achieving a large FOV comes with the tradeoff of resolution, as reducing the magnification to increase the FOV may reduce the achievable resolution when the full-width at half maximum (FWHM) of the point spread function (PSF) is no longer properly sampled by the effective sampling rate considering the Nyquist-Shannon Sampling Theorem, described as:

$$\frac{PSF_{FWHM}}{sampling\ rate_{eff}} \geq 2 \qquad (1)$$

In the case where **Equation 1** does not hold true, resulting in undersampled images, improvements to the PSF will not improve the achievable resolution, as the digital sampling rate is insufficient to capture any such improvement [2]. In this context, improving the SBP of an undersampled imaging system requires increasing the digital sampling rate while preserving the system's original FOV. While methods have been developed to increase the spatial sampling rate by means of subpixel sampling, the reconstruction quality depends highly on the precision of step size used in the system [3,4]. Another method, Fourier ptychography [5], modulates the illumination pathway to induce phase differences across the sample before computationally improving resolution while maintaining FOV, but this is impractical for systems where the illumination pathway is inextricable from the imaging method, such as confocal [2, 6] and light-sheet microscopy [4, 7-9]. In addition, while image stitching is a commonly used method of increasing the spatial bandwidth of the final image by fusing a set of images constrained by the SBP in the aforementioned methods, the stitching process can often induce artifacts along the boundaries of the individual images [10]. Finally, our proposed strategy is a feed-forward method, in contrast to iterative refinement based on a high-quality ground truth dataset used in content-aware and deep learning methods. This approach minimizes the data variation and experimental bias that may result from a cross modality setting [11]. Thus, a non-iterative method to improve the spatial sampling rate without compromising the system's FOV, while remaining independent of the illumination pathway and stage/motor precision during translation, is an unmet need.

In this Letter, we report a method that includes a subpixel shifting mechanism along with its reconstruction algorithm to improve spatial resolution by ~42% while preserving the FOV of the undersampled system, resulting in a greater than 2-fold improvement to the effective SBP. We imaged a USAF 1951 target (R1DS1N, ThorLabs) using a home-built microscope configured for widefield use [8, 9], whose detection objective's NA is 0.25. The system's magnification was 3.2X and the binning was 4x4, such that the effective sampling rate was 8 μm, representing an undersampled system. To improve the SBP, we increased the spatial sampling rate through sample shifting by subpixel increments (e.g. 1/16, 1/8, 3/16, etc. of our system's sampling rate) thereby capturing sets of up to 8 SBP-constrained images within one shift range, respectively. The phase correlation (PC) and shift-and-add (SAA) techniques were used to reconstruct high-resolution, large-FOV images before deblurring via Richardson-Lucy deconvolution, which is known to remove artifacts and noises [12]. The deblurring step removes the discrete motion blur artifact caused by sample shifting and image fusion. The reconstruction algorithm, coined PC + SAA, requires that the sample to be imaged is laterally shifted in intervals smaller than the effective sampling rate, with an image being captured after each consecutive shift. The physical sample is translated using subpixel shifts of size $(\Delta x, \Delta y)$, as demonstrated in **Figure 1a**. While the values of

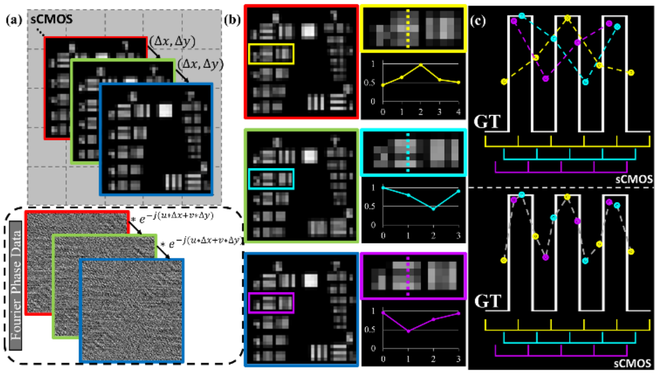

Fig 1. Effect of subpixel shifting on data acquisition and data fusion. (a) Above: Schematic depicting the sample shift by amounts $(\Delta x, \Delta y)$, which need not be exact. Below: The resulting effect on the phase data in the frequency domain after each shift. (b) Left: Images depicting the intensity variations caused by subpixel shifts. Right: Zoomed-in portions of note with accompanying intensity plots for comparison of different groups on the USAF target. (c) Schematic of the pixel intensities of Group 6, Element 3, shifted to match relative position. Above: considered as separate trends. Below: considered as a single continuously sampled trend. GT: ground truth.

$(\Delta x, \Delta y)$ can be approximated from the input motor step size [3,4], the inherent imprecision of the system's motors compound during shifting, producing approximations of $(\Delta x, \Delta y)$ whose tolerance multiplicatively deviates from the intended shift size with each applied shift. This translation produces significant intensity variations, highlighted by the representative yellow, cyan, and purple-bordered sections of the images in **Figure 1b**. These variations occur due to several factors, including desired variations caused by the changing alignment of the sample within the sensor matrix, as well as the relationship between the spatial sampling rate and the frequencies present in the sample, and undesired variations caused by noise contributions and motor imprecision. Though the system cannot resolve below 7.8 µm in a single image, the subpixel shifts allow for the fulfillment of Nyquist-Shannon guidelines by increasing the spatial sampling rate, allowing for a higher-resolution reconstruction. Thus, the importance of these intensity variations is revealed in **Figure 1c**, which plots the intensities captured from the shifted images containing unique intensity variation patterns with respect to Group 6, Element 3 of a USAF 1951 target, which corresponds to a resolution of 6.2 µm. Given the system's best achieved resolution of 7.8 µm, it is infeasible that this portion of the USAF target could be resolved within a single image, a limitation imposed by the Nyquist-Shannon Sampling Theorem. This is visualized by none of the individual trendlines being able to display all three bars of the underlying signal of the target (**Figure 1c, above**). However, if these intensities are plotted sequentially, rather than independently, regarding the relative pixel shift given it, the resulting trend approximates the ideal function that is found in Group 6, Element 3 (**Figure 1c, below**).

After capturing a series of subpixel-shifted images, the images are then upscaled using pixel duplication, to preserve the original captured signal, before being post-processed by the reconstruction algorithm, which registers, upscales, shifts, and merges the low-resolution base images into a cohesive, high-resolution image, elaborated in **Figure 2**. The PC algorithm [11-14] registers each image in reference to the first image, estimating the shifting parameter needed to align the shifted image with the reference image, using the Fourier Shift Theorem, defined as:

$$f_2(x,y) = f_1(x - \Delta x, y - \Delta y) \qquad (2)$$

$$F_2(u,v) = F_1(u,v)e^{-j(u*\Delta x + v*\Delta y)} \qquad (3)$$

where $f_2(x,y)$ represents the shifted function $f_1(x,y)$ after being shifted by $(\Delta x, \Delta y)$, $F_1(u,v)$ and $F_2(u,v)$ are the Fourier Transforms of $f_1(x,y)$ and $f_2(x,y)$, (x,y) are spatial coordinates within functions $f_1(x,y)$ and $f_2(x,y)$, and (u,v) are frequency coordinates within functions $F_1(u,v)$ and $F_2(u,v)$ [11-14]. This relation specifies that the effect of the spatial shift $(\Delta x, \Delta y)$ is solely present in the phase information in the Fourier domain and can be extracted by determining the value of the phase difference between the two functions, $e^{-j(u*\Delta x + v*\Delta y)}$. This phase difference can be isolated in the Fourier domain by calculating the Cross Power Spectrum (CPS), given by:

$$e^{-j(u*\Delta x + v*\Delta y)} = \frac{F_1(u,v)F_2^*(u,v)}{|F_1(u,\ v)F_2^*(u,v)|} \qquad (4)$$

where the asterisk (*) denotes the complex conjugate. It is noteworthy that PC is intensity-invariant, relying solely on phase data to achieve registration [13], allowing versatility for both high and low-photon budget applications. In addition, by filtering the two frequency spectra with an ideal high-pass filter, we further refine the precision and robustness of the correlation, emphasizing edge-based features preserved between images. Alternatively, other filters including Gaussian and Butterworth filters could be used to reject noise contributions from impeding registration accuracy. The CPS is then converted back into the spatial domain via the Inverse Fourier Transform (IFT), where the resulting Inverse Cross Power Spectrum (ICPS) isolates the pixel-precision shift $(\delta x, \delta y)$ based on the coordinates of the maximum correlation value, modeled as a unit impulse function in the discrete domain [13], as seen in **Figure 2a**. Since traditional PC is only precise to the region of a pixel, the centroid-based method is utilized in this algorithm to estimate the subpixel-precision shift. The centroid-based method is a localized center of mass calculation weighted by the correlation value of the main peak and surrounding sub-peaks of the ICPS, defined as:

$$\left(\widetilde{\Delta x} = \frac{\sum_{m=\delta x-c}^{\delta x+c} mI_{icp}(m,n)}{\sum_{m=\delta x-c}^{\delta x+c} I_{icp}(m,n)}, \widetilde{\Delta y} = \frac{\sum_{n=\delta y-c}^{\delta y+c} nI_{icp}(m,n)}{\sum_{n=\delta y-c}^{\delta y+c} I_{icp}(m,n)}\right) \qquad (5)$$

where $(\widetilde{\Delta x}, \widetilde{\Delta y})$ are the centroid-estimated coordinates around the pixel-precision spatial coordinates of the ICPS, $(\delta x, \delta y)$, m and n are general spatial coordinates in the ICPS, I_{icp} refers to the correlation intensity of the ICPS, and c is an arbitrary boundary parameter. In our experience, a c value of 5 allowed for acceptable precision for our sample and shifting amount. After calculating the centroid-estimated shift $(\widetilde{\Delta x}, \widetilde{\Delta y})$, these registered images are then combined using the SAA method [15, 16], which shifts the relative position of data within the image by $(\widetilde{\Delta x}, \widetilde{\Delta y})$, then adds the image to a cumulative sum of images until the entire registered stack is combined, as shown in **Figure 2b**. Thus, the process of acquisition, image capture, upsampling, phase correlation, and data fusion are summarized by **Figure 2c**.

To demonstrate the effectiveness of PC + SAA, a 1951 USAF target was imaged using subpixel shifting before being reconstructed. The images shown in **Figure 3a** have had a sample shift of 3/16 of a pixel in the x and y-directions before being reconstructed. This quantity equals 1.5 ± 0.25 µm, as our digital sampling rate is 8 µm for this demonstration. With image registration being provided by PC, image enlargement using pixel

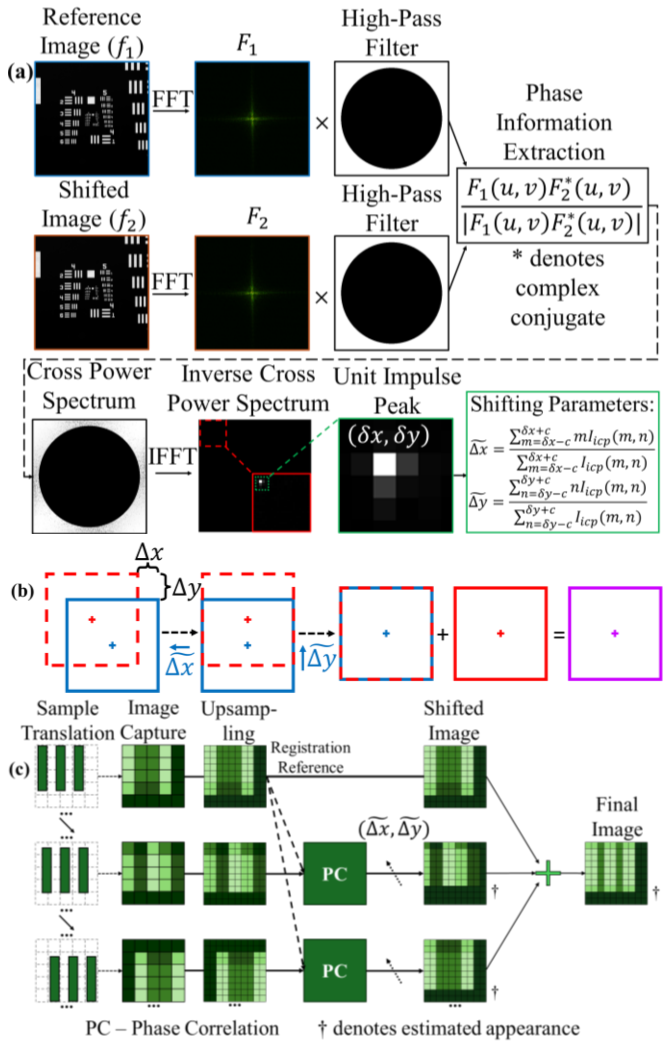

Fig 2. PC + SAA algorithm overview. (a) Flowchart of the phase-correlation process, which yields the subpixel precision shifting coordinates $(\widetilde{\Delta x}, \widetilde{\Delta y})$. (b) Schematic of the SAA procedure, where the shifted image (blue) is shifted by $(\widetilde{\Delta x}, \widetilde{\Delta y})$ to align with the reference image (red), before being added to the reference image to create a composite of the two. (c) Overview of the PC + SAA method, wherein the translated sample is captured, upsampled, phase correlated, shifted by $(\widetilde{\Delta x}, \widetilde{\Delta y})$, and additively merged into a coherent, high-resolution image.

duplication, and image merging using SAA, the intensity differences between subsequent subpixel shifted images allow for substantial resolution improvement, as is demonstrated in **Figure 3.** Previously, Group 6, Element 1 was the best resolvable element, corresponding to a digital resolution of 7.8 µm, but our PC + SAA algorithm was able to resolve down to Group 6, Element 3, corresponding to a digital resolution of 6.2 µm, resulting in an improvement of ~26% (**Figure 3b**). After 100 iterations of deblurring, the resolving power increased to reliably elucidate Group 6, Element 4, denoting a digital resolution of 5.5 µm and equal to a ~42% improvement (**Figure 3c**) and (**Visualization 1**). It is notable that the FOV is preserved across the low-resolution images and the high-resolution reconstruction, maintaining its original ~4mm × 4mm physical size despite the improvement to resolution. This preservation results in an improvement to the SBP of 1.58-fold with PC + SAA alone, and 2.01-fold after deblurring. Resolution was

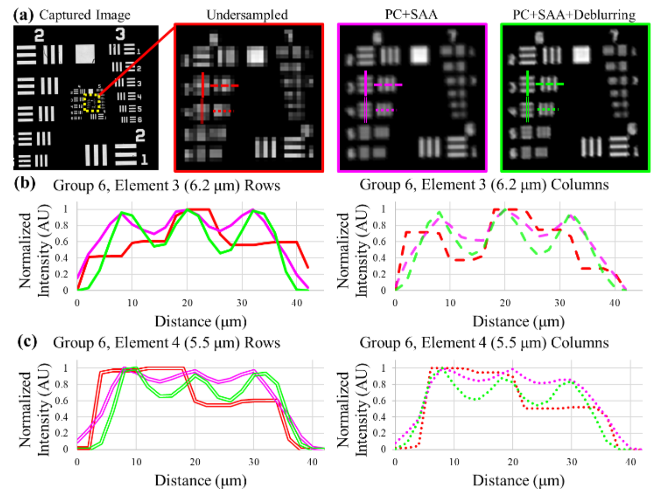

Fig 3. Resolution improvement from subpixel-shift sampling and PC + SAA reconstruction. (a) An example image captured by the system, with zoomed in portions representing the areas of interest in the under-sampled image (red), as well as post-processed PC + SAA (magenta) and PC + SAA + Deblurring (green) images. (b) Line profiles taken from Group 6, Element 3 rows (left) and columns (right). (c) Line profiles taken from Group 6 Element 4 rows (left) and columns (right).

determined using the Rayleigh criterion, wherein a valley-to-peak ratio of no more than 80% demonstrated a resolved set of elements [19].

The resolution improvement exhibited by the PC + SAA method is a function of the shifting size and the number of images captured. Shifting size determines the distance between sequential sub-sampled points, affecting the spatial sampling rate, and the latter represents the number of shifts captured, determining the total number of sub-sampled points considered. The trends in **Figure 4** imply an optimal value for both parameters, in that each shifting increment achieves the same minimum resolution after $\sim \frac{pixel\ size}{shifting\ parameter}$ images. **Figure 4a** highlights the benefit of deblurring, as even though it failed to converge to the maximum achieved resolution after 8 images, the deblurring algorithm produced significantly improved results after 5 images. **Figure 4b** presents the first shifting parameter that converges to its best achieved resolution after 8 images. However, as the PC+SAA sampling method increases the imaging time for a sample multiplicatively per image, it is necessary to minimize the number of shifts, and therefore images, while still reliably achieving the optimal resolution improvement. For example, the 1/2-pixel shift case (**Figure 4f**) recovers the minimum achieved resolution after 2 images, but the standard deviation of achieving this is ±0.34µm before deblurring and ±0.86µm after. The 3/8-pixel shift case (**Figure 4e**) performs similarly at 3 images before deblurring at ±0.39µm but improves after deblurring to ±0.70µm. The 1/4-pixel shift case (**Figure 4d**) continues this trend with 4 images at ±0.16µm before deblurring and ±0.58 µm after. Finally, the 3/16-pixel shift case (**Figure 4c**) recreates the minimum resolution after 6 images but does so with a standard deviation of ±0.00µm before deblurring and ±0.17 µm after, showing an increase in reliability using smaller shifting parameters. Thus, we present that, for photostable samples, 4 images with a shifting parameter of 1/4-pixel provides the best opportunity to reliably achieve optimal resolution improvement, and 2 images with a 1/2-pixel shifting

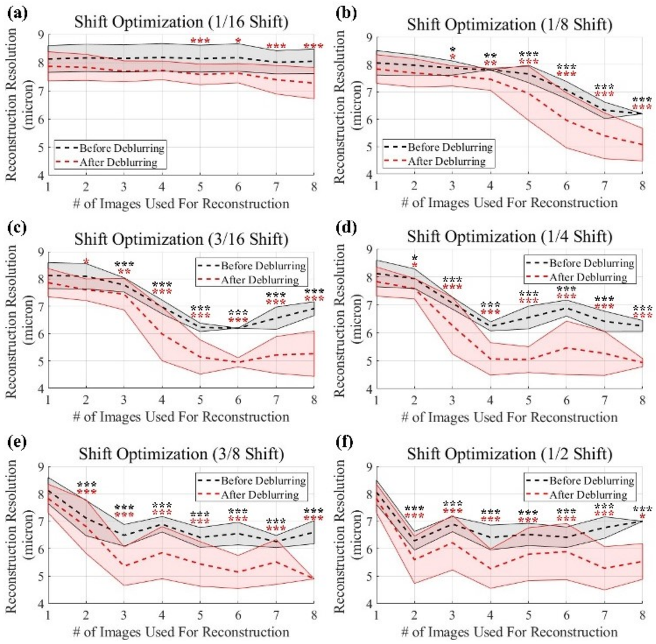

Fig. 4. Resolution as a function of the number of images considered for PC + SAA reconstruction before (black) and after (red) deblurring with respect to shifting increments of (a) 1/16, (b) 1/8, (c) 3/16, (d) 1/4, (e) 3/8, and (f) 1/2-pixel incremental shifts. Dashed lines represent mean values, shaded areas represent ± standard deviation. Unpaired, one-tail T-tests were performed against single image data of the respective trends. * denotes $p < 0.05$, ** denotes $p < 0.01$, and *** denotes $p < 0.001$.

parameter provides beneficial results if photo-bleaching or photo-damage is a concern.

In this Letter, we report a subpixel sampling method and novel reconstruction algorithm using PC registration and SAA image fusion for a resolution increase of up to ~26% without penalty to the resulting FOV, increasing the information carrying capacity of an under-sampled system ~1.58-fold. Additionally, deblurring the PC+SAA images with a discretized motion-blur kernel via Richardson-Lucy deconvolution further enhances the resolution by up to ~42% of the original resolution, thus increasing the system's SBP more than 2-fold. By virtue of its feed-forward, non-iterative design, PC+SAA also demonstrates a reconstruction time of ~60 seconds to process a stack of 16 images each 512x512 pixels in size, then ~30 seconds for 100 iterations of deconvolution, using a workstation with a 2.6 GHz CPU and 64 GB DDR4 RAM. The proposed method, PC + SAA, addresses the effects of digital sampling on image acquisition with the ability to improve resolution. By utilizing the PC image registration method, a computational registration algorithm, the registration precision is not bound by the translational precision of the system, and using the SAA image fusion method, a computational fusion algorithm, aligns the effects of intensity variations across subpixel shifts. Though image quality enhancement from optical resolution is not expressly addressed by this method, established methods that aim to correct optics-limited resolution can be applied to the reconstructed image to address image degradation further. Since PC + SAA and optics-oriented reconstruction methods address different limitations of conventional optical microscopy, their interactions do not behave antagonistically. While the PSF of the system cannot be mitigated by the PC+SAA technique, this technique is able to increase the spatial sampling rate by up to twice the system's previous capability, leading to the demonstrated resolution improvement. This threshold marks the frequency where sample peaks can coexist within a single pixel of the original image, preventing them from being separable by a low-intensity valley across at least three pixels. Current limitations to achieving this theoretical limit include registration precision and additive background signal during image fusion. We note that the use of centroid localization in our PC algorithm may present difficulties in achieving this theoretical limit, prompting the development of a more precise PC registration algorithm in the future. We demonstrate that the PC+SAA framework provides much-needed resolution improvements to otherwise undersampled systems [8, 9], which increases the quality of images produced with the system and the amount of available information that can be encoded therein. By decoupling the reconstruction algorithm from the system's illumination pathway and motor stage precision, PC+SAA can be used in a variety of optical imaging systems and applications. We intend to extend our work in PC+SAA towards 3D volumetric image reconstruction of murine, zebrafish, and organoid models.

Funding. This study was supported by NIH R00HL148493, R01HL162635, NSF 2326628, and the UT Dallas STARS program.

Disclosures. The authors declare no conflicts of interest.

Data Availability. Data underlying the results presented in this paper are not publicly available at this time but may be obtained from the authors upon reasonable request.

REFERENCES:

1. M. A. Neifeld, *Opt. Lett.*, **23**, 1477 (1998).
2. J. B. Pawley, *Handbook Of Biological Confocal Microscopy*, 3rd ed. (Springer US, 2006).
3. H. Lee, J. Kim, J. Kim, *et al.*, *Opt. Express*, **29**, 29996–30006 (2021).
4. P. Fei, J. Nie, J. Lee, *et al.*, *Adv. Photonics*, **1**, 1 (2019).
5. G. Zheng, C. Shen, S. Jiang, *et al.*, *Nat. Rev. Phys.*, **3**, 207–223 (2021).
6. J. Jonkman, C. M. Brown, G. D. Wright, *et al.*, *Nat. Protoc.*, **15**, 1585–1611 (2020).
7. E. H. K. Stelzer, F. Strobl, B.-J. Chang, *et al.*, *Nat. Rev. Methods Prim.*, **1**, 73 (2021).
8. O. Sodimu, M. Almasian, P. Gan, *et al.*, *J. Biophotonics*, **16**, e202200278 (2023).
9. M. Almasian, A. Saberigarakani, X. Zhang, *et al.*, *J. Vis. Exp.*, **205**, e66707 (2024).
10. J. Chalfoun, M. Majurski, T. Blattner, *et al.*, *Sci. Rep.*, **7**, 4988 (2017).
11. M. Weigert, U. Schmidt, T. Boothe, *et al.*, *Nat. Methods*, **15**, 1090–1097 (2018).
12. M. Makarkin and D. Bratashov, *Micromachines*, **12**, (2021).
13. X. Tong, K. Luan, U. Stilla, *et al.*, *IEEE J. Sel. Top. Appl. Earth Obs. Remote Sens.*, **12**, 4062–4081 (2019).
14. B. S. Reddy and B. N. Chatterji, *IEEE Trans. Image Process.*, **5**, 1266–1271 (1996).
15. A. Alba, J. F. Vigueras-Gomez, E. R. Arce-Santana, *et al.*, *Comput. Vis. Image Underst.*, **137**, 76–87 (2015).
16. H. Foroosh, J. B. Zerubia, and M. Berthod, *IEEE Trans. Image Process.*, **11**, 188–200 (2002).
17. W. G. Bagnuolo, *Opt. Lett.*, **10**, 200–202 (1985).
18. S. Farsiu, D. Robinson, M. Elad, *et al.*, *Proc. SPIE - Int. Soc. Opt. Eng.*, **5203**, (2003).
19. J. Fuenzalida, A. Hochrainer, G. B. Lemos, *et al.*, *Quantum*, **6**, 646 (2020).

REFERENCES:

1. M. A. Neifeld, "Information, resolution, and space–bandwidth product," Opt. Lett. **23**, 1477 (1998).
2. J. B. Pawley, Handbook Of Biological Confocal Microscopy, 3rd ed. (Springer US, 2006).
3. H. Lee, J. Kim, J. Kim, P. Jeon, S. A. Lee, and D. Kim, "Noniterative sub-pixel shifting super-resolution lensless digital holography," Opt. Express **29**, 29996–30006 (2021).
4. P. Fei, J. Nie, J. Lee, Y. Ding, S. Li, H. Zhang, M. Hagiwara, T. Yu, T. Segura, C. M. Ho, D. Zhu, and T. K. Hsiai, "Subvoxel light-sheet microscopy for high-resolution high-throughput volumetric imaging of large biomedical specimens," Adv. Photonics **1**, 1 (2019).
5. G. Zheng, C. Shen, S. Jiang, P. Song, and C. Yang, "Concept, implementations and applications of Fourier ptychography," Nat. Rev. Phys. **3**, 207–223 (2021).
6. J. Jonkman, C. M. Brown, G. D. Wright, K. I. Anderson, and A. J. North, "Tutorial: guidance for quantitative confocal microscopy," Nat. Protoc. **15**, 1585–1611 (2020).
7. E. H. K. Stelzer, F. Strobl, B.-J. Chang, F. Preusser, S. Preibisch, K. McDole, and R. Fiolka, "Light sheet fluorescence microscopy," Nat. Rev. Methods Prim. **1**, 73 (2021).
8. O. Sodimu, M. Almasian, P. Gan, S. Hassan, X. Zhang, N. Liu, and Y. Ding, "Light sheet imaging and interactive analysis of the cardiac structure in neonatal mice," J. Biophotonics **16**, e202200278 (2023).
9. M. Almasian, A. Saberigarakani, X. Zhang, B. Lee, and Y. Ding, "Light-Sheet Imaging to Reveal Cardiac Structure in Rodent Hearts," J. Vis. Exp. **205**, e66707 (2024).
10. J. Chalfoun, M. Majurski, T. Blattner, K. Bhadriraju, W. Keyrouz, P. Bajcsy, and M. Brady, "MIST: Accurate and Scalable Microscopy Image Stitching Tool with Stage Modeling and Error Minimization," Sci. Rep. **7**, 4988 (2017).
11. M. Weigert, U. Schmidt, T. Boothe, A. Müller, A. Dibrov, A. Jain, B. Wilhelm, D. Schmidt, C. Broaddus, S. Culley, M. Rocha-Martins, F. Segovia-Miranda, C. Norden, R. Henriques, M. Zerial, M. Solimena, J. Rink, P. Tomancak, L. Royer, F. Jug, and E. W. Myers, "Content-aware image restoration: pushing the limits of fluorescence microscopy," Nat. Methods **15**, 1090–1097 (2018).
12. M. Makarkin and D. Bratashov, "State-of-the-Art Approaches for Image Deconvolution Problems, including Modern Deep Learning Architectures," Micromachines **12**, (2021).
13. X. Tong, K. Luan, U. Stilla, Z. Ye, Y. Xu, S. Gao, H. Xie, Q. Du, S. Liu, X. Xu, and S. Liu, "Image Registration with Fourier-Based Image Correlation: A Comprehensive Review of Developments and Applications," IEEE J. Sel. Top. Appl. Earth Obs. Remote Sens. **12**, 4062–4081 (2019).
14. B. S. Reddy and B. N. Chatterji, "An FFT-based technique for translation, rotation, and scale-invariant image registration," IEEE Trans. Image Process. **5**, 1266–1271 (1996).
15. A. Alba, J. F. Vigueras-Gomez, E. R. Arce-Santana, and R. M. Aguilar-Ponce, "Phase correlation with sub-pixel accuracy: A comparative study in 1D and 2D," Comput. Vis. Image Underst. **137**, 76–87 (2015).
16. H. Foroosh, J. B. Zerubia, and M. Berthod, "Extension of phase correlation to subpixel registration," IEEE Trans. Image Process. **11**, 188–200 (2002).
17. W. G. Bagnuolo, "Image restoration by the shift-and-add algorithm," Opt. Lett. **10**, 200–202 (1985).
18. S. Farsiu, D. Robinson, M. Elad, and P. Milanfar, "Robust Shift and Add Approach to Super-Resolution," Proc. SPIE - Int. Soc. Opt. Eng. **5203**, (2003).
19. J. Fuenzalida, A. Hochrainer, G. B. Lemos, E. A. Ortega, R. Lapkiewicz, M. Lahiri, and A. Zeilinger, "Resolution of Quantum Imaging with Undetected Photons," Quantum **6**, 646 (2020).